Frequency Adaptive Repetitive Control of New Energy Grid-Connected Inverter Based on Improved IIR

Pu Liu, Cong Wang, Yingwei Zhang, Yan Liang, Yibo Cui, and Jie Fang

***Abstract*—This article proposes a frequency adaptive repetitive control (FARC) strategy based on an improved infinite impulse response (IIR) filter for new energy grid-connected inverters. By changing the parameters of the IIR filter in real time, the FARC based on the improved IIR filter can achieve frequency adaptation. Considering the narrow effective gain bandwidth of repetitive control (RC), the tracking accuracy of RC is more sensitive to frequency fluctuations. Aiming at this problem, a method of adaptive delay number is proposed, in the case of a fixed sampling period. The method can update the delay coefficient of the filter in real time by introducing a new ladder structure in the IIR filter based on the Thiran algorithm, making the proposed FARC capable of frequency adaptation. The introduced ladder structure is easy to design and can address the complex problem of Thiran filter digital circuit implementation effectively. To verify the feasibility of the scheme, the improved frequency adaptive repetitive controller is theoretically analyzed, and the effectiveness and accuracy of the proposed FARC are verified by simulation and experiments.**

***Index Terms*—Fractional order delay, frequency adaptation repetitive control (FARC), ladder structure, Thiran filter.**

I. Introduction

AS THE core component of the new energy power generation system, the grid-connected inverter is the power conversion interface between the new energy power generation system and the power grid, aiming to convert the obtained dc power into ac power for grid connection, but introduces harmonics current into the power grid at the same time [1], [2].

To alleviate the harmonic injection and reduce the distortion rate of the grid-connected current, various linear and nonlinear current control strategies are introduced in the control system [3], [4], [5]. Among them, PI control [3] and dead-beat (DB) control [4] are widely used for their simple implementation and better dynamic performance. However, PI control has a limited impact on harmonic suppression, and DB control is very sensitive to uncertain parameters of the controlled object. Both proportional resonance control [5] and repetitive control (RC) [6] can introduce high resonance gain at specific frequencies to accomplish error-free tracking, but one resonator can only target a single harmonic. The proportional multiple resonant (PMR) controller can compensate for the specific harmonic frequencies of the grid current. However, the amount of calculation of PMR is large, the control system is more complicated, and the stability of the system is easily affected.

RC based on the principle of internal mode can introduce resonant peaks at the fundamental frequency and its multiplier. By introducing a periodic delay on the forward channel and constructing the positive feedback, RC can achieve efficient suppression of any integer-order harmonics and meet the error-free tracking at arbitrary integer harmonic currents. As a consequence, RC is extensively used in inverters [7], [8], [9], active power filters [10], [11], permanent magnet synchronous motors [12], [13], and other equipment. When large-scale new energy sources are connected to the power grid, the grid frequency will fluctuate, and the steady-state performance of the grid-connected inverter based on the RC strategy will decrease due to the narrow gain bandwidth of RC at the resonant frequency.

To address the issue that the control effect of RC decreases with frequency fluctuation, the stability coefficient Q can be reasonably designed to reduce the sensitivity of the system at frequency fluctuations. Zhang et al. [14] compared the magnitude–frequency characteristics when Q was selected as a constant or a zero-phase comb filter after introducing Q, however, the introduction of Q value sacrifices the high gain at the resonance peak. To achieve the purpose that the resonant frequency of RC can track the variation of the grid frequency in time, the existing methods mostly consider the adaptive sampling period and the number of adaptive delays number N, making the internal model delay of the RC equal to the power grid fundamental wave period. Considering the complexity and high cost of hardware implementation of variable sampling control [15] systems, lots of studies focus on changing the number of delays N [16], [17]. It is pointed out in [18] that introducing filters into each delay link in the internal mode of RC can realize variable fractional delay (FD) compensation, to change the resonant frequency of

Manuscript received 31 May 2022; revised 24 November 2022 and 9 March 2023; accepted 28 April 2023. Date of publication 11 May 2023; date of current version 21 June 2023. This work was supported in part by the Science and Technology Development Project of Henan Province (222102220089) and in part by the Major Science and Technology Special Program of Henan Province (221100240500). Recommended for publication by Associate Editor H. L. Ginn. *(Corresponding author: Jie Fang.)*

Pu Liu, Cong Wang, Yan Liang, Yibo Cui, and Jie Fang are with the School of Electric and Information Engineering, Zhengzhou University of Light Industry, Zhengzhou 450002, China (e-mail: liupu1984@stu.xjtu.edu.cn; wangc_zzuli@163.com; yanliang506@hotmail.com; 332101020013@email.zzuli.edu.cn; 332101020006@email.zzuli.edu.cn).

Yingwei Zhang is with the Computer and Electrical Engineering, University of Shanghai for Science and Technology, Shanghai 200093, China (e-mail: 202421579@st.usst.edu.cn).

Color versions of one or more figures in this article are available at https://doi.org/10.1109/TPEL.2023.3274185.

Digital Object Identifier 10.1109/TPEL.2023.3274185

the internal mode and guarantee the high resonance peak gain of the system.

Linear phase FIR filter is simple in structure and convenient to design, so the FD has been implemented with FIR filter in most existing RCs [19], [20], [21], [22]. Among them, the Lagrange interpolation has become a common interpolation method for designing FIR filter coefficients due to its easy implementation and the maximally flat passband characteristics of its frequency response [23], [24], [25]. In [26], the weighted-least-square method is adopted to design the low-pass FIR filter approximating its ideal frequency response, which has a wider pass bandwidth than the Lagrange interpolation method and can guarantee the tracking precision of the RC in high-speed scanning. In addition, the Lagrange interpolation filter is a piecewise polynomial, which can be implemented using the Farrow structure. The Farrow structure can further improve the FIR filter based on the Lagrange interpolation algorithm, making the system more efficient [27]. In [28], the Lagrange interpolation FD filter based on Taylor series expansion with the Farrow structure is used to accurately approximate the FD, where each subfilter can be designed offline, reducing the computational burden on the controller. In [29], a fractional filter based on Newton's structure is proposed to approximate the FD, which structure is transformed from the Farrow structure. These filter coefficients are constant and do not need to be adjusted online, which greatly reduces the calculation amount and implementation complexity.

There is a common problem in the above methods of implementing frequency adaptive RC (FARC) using FIR filters, that is, the balance between FIR filter order and implementation complexity is required [30]. The higher the order, the higher the tracking accuracy, but the implementation complexity and calculation time of the system also increase correspondingly [31], [32]. Conversely, the lower the order, the lower the tracking accuracy and the lower the resource occupancy of the system [33]. Under the same tracking accuracy, the infinite impulse response (IIR) filter requires less order than the FIR filter [34]. Moreover, compared with the FIR filter, the IIR filter can provide better high-frequency attenuation with lower order [35].

Considering the application scenario of RC of internal model delay, there are design requirements for the phase frequency response of the filter. To ensure a unity amplitude response over the entire frequency range, the IIR filter is usually designed in the form of an all-pass filter, which reduces the design difficulty of the filter [36]. To ensure the stability of the IIR filter, the Thiran method with maximum flatness characteristics has been widely used [37], [38]. In [39], [40], and [41], the IIR filter is used to implement FARC, and the direct-form structure of the Thiran formula is used to determine the IIR filter coefficient, which achieves the same accuracy using fewer orders and better high-frequency tracking accuracy, but the direct-form structure of Thiran filter is complicated.

The contributions of this article are as follows. First, an improved FARC scheme is proposed in this article. This FARC scheme improves the complex problem of IIR filter implementation based on Thiran approximation, by using a novel ladder structure that is based on continued fraction derivation. Furthermore, in Section II, the plug-in RC structure is briefly described and the realization method of the proposed ladder structure is introduced. Section III applies the above-mentioned ladder structure to the grid-connected inverter and designs the parameters based on the stability constraints of RC. Finally, in Section IV, simulations and experiments are carried out on a three-phase grid-connected inverter platform, and the results verify the accuracy and effectiveness of the proposed adaptive RC scheme.

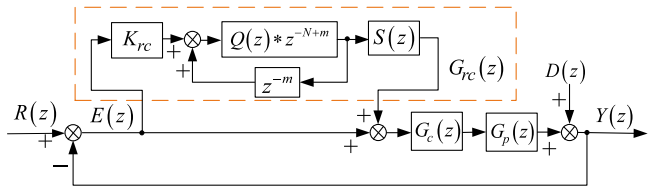

Fig. 1. Plug-in RC system.

II. Improved Frequency Adaptive Repetitive Control

A. Plug-in Repetitive Control

Fig. 1 shows the structure block diagram of plug-in RC [15], [16]. In this topology, $G_p(z)$ is the controlled object, $G_c(z)$ is the state feedback part, $G_{\mathrm{rc}}(z)$ is the repetitive controller, and Q is the internal model stability coefficient, which usually uses a low-pass filter Qz or a constant Qc less than 1. z^m is used to compensate for the phase of the correction object, and the low-pass filtering part $S(z)$ is used to reduce the high-frequency gain and improve the high-frequency steady-state margin of the system. The loop gain of RC is K_{rc}, which can change the system convergence speed.

Without considering z^m, the transfer function of RC [15] can be expressed as

$$G_{\mathrm{rc}}(z) = K_{\mathrm{rc}} \frac{z^{-N}Q}{1 - z^{-N}Q} \cdot S(z). \tag{1}$$

In (1), $N = T_0/T_s$, where T_0 is the fundamental period and T_s is the sampling period of the system.

RC introduces the resonant peak at the fundamental frequency and its multiples, by introducing a periodic delay on the forward channel and constructing positive feedback, and then achieves the error-free tracking of any integer-order harmonic current. However, in the actual project, the power system is affected by the grid-connected of the large-scale new energy power generation system, during normal working, and there will have frequency fluctuation which will lead to a deviation between the internal model delay N and the power grid fundamental wave period, and the control effect will be poor. On the basis of (1), in the condition without considering the influence of $S(z)$, the relationship between the resonance bandwidth σ and the stability coefficient Q in the s domain is as follows:

$$\sigma = -{}^{1}\!/_{T_0} \ln Q_{\mathrm{c}} \tag{2}$$

where Q is the constant Qc. It can be known from (2) that the resonance bandwidth of the fundamental wave integer times frequency is inversely proportional to Qc. Consequently, the cost of increasing the resonance bandwidth is to reduce the Qc value, meaning that reduces the gain at the resonance peak, which will lead to a decrease in the steady-state error accuracy.

Furthermore, when the stability coefficient Q takes the low-pass filter Qz, Qz cannot be directly brought into formula (2), but within the system cutoff frequency range, Qz can be considered to be constant 1, so the effect of using Qz also satisfies the above formula.

B. Improved Thiran Filter-Ladder Structure

To ensure that the repetitive controller still maintains high gain at the fundamental wave when the grid side frequency changes, an RC strategy based on the ladder structure Thiran FD is proposed. At the grid frequency changes, $N = T_0/T_s = N_i + D$, where N_i is an integer part and D is the fractional part. The delay of the fractional part z^{-D} can be approximated by the IIR filter based on the Thiran approximation method, and frequency characteristics of z^{-D} is given as follows:

$$\begin{cases} \left|z^{-D}\right| = 1 \\ \angle z^{-D} = \angle e^{-sDT_s} \end{cases}. \tag{3}$$

From (3), it can be seen that the amplitude–frequency response of z^{-D} is 0 dB, and the phase–frequency response of z^{-D} has linear characteristics, hence the IIR filter in the all-pass filter is selected to approximate the fractional order delay. Compared with the FIR filter in the same order, the IIR filter has better amplitude–frequency characteristics in the low-frequency band.

In general, IIR filters based on the direct form of the Thiran algorithm are used to approximate FD [36]. The transfer function of the N_r-order IIR filter [38], [39], [40] is as follows:

$$A_{\mathrm{FD}}(z) = \frac{a_{N_r} + a_{N_r-1}z^{-1} + \cdots + z^{-N_r}}{1 + a_1 z^{-1} + \cdots + a_{N_r}z^{-N_r}}. \tag{4}$$

The all-pass filter coefficients by Thiran formula [38], [39], [40] are given by

$$a_k = \frac{(-1)^k N_r!}{k!(N_r-k)!}\prod_{n=0}^{N}\frac{D - N_r + n}{D - N_r + n + k}. \tag{5}$$

In (5), $k = 1, 2, \ldots, N_r$, $D = N_r + d$, and the condition for the establishment of (5) is $D > N_r - 1$. Generally speaking, the best range of Thiran digital delay is $[N_r - 0.5,\ N_r + 0.5]$, so d is between $[-0.5,\ 0.5]$.

Considering the hardware implementation of digital circuits, compared with the direct-form structure [36], this article uses a ladder structure based on continuous fractions to realize the Thiran filter.

The general form of the continuous fraction [42], [43] is

$$X_0 + \cfrac{Y_1}{X_1 + \cfrac{Y_2}{X_2 + \cfrac{Y_3}{X_3 + \ddots}}}. \tag{6}$$

In (6), X_i and Y_i are called elements of the continuous fraction. Usually for the convenience of writing, (6) is written as a compact form of the following equation:

$$X_0 + \frac{Y_1}{X_1 +}\frac{Y_2}{X_2 +}\frac{Y_3}{X_3 +}\cdots \tag{7}$$

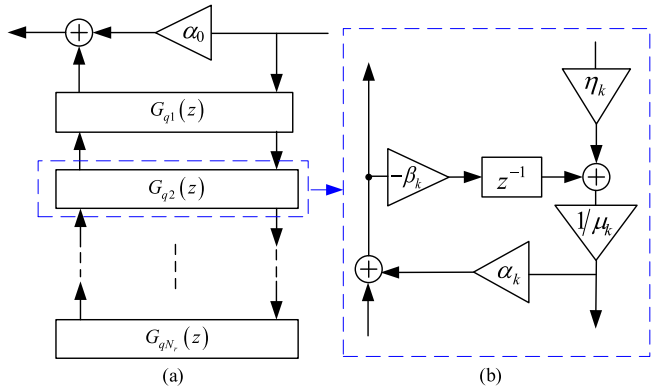

Fig. 2. Ladder structure of the filter. (a) Ladder-shaped main body. (b) Details in the bar.

The continued fraction form of x^{-y} is as follows:

$$x^{-y} = 1 - \frac{y}{\dfrac{x}{x-1} +}\frac{y-1}{2-}\frac{y+1}{3\dfrac{x}{x-1} +}\frac{y-2}{2-} \cdots \frac{y+k-1}{(2k-1)\dfrac{x}{x-1} +}\frac{y-k}{2-}\cdots. \tag{8}$$

Substituting $x = z^{-1}$ and $y = -D$ into (8), the expression form of z^{-D} is shown in the following equation (the details of the derivation are given in Appendix):

$$z^{-D} = 1 + \frac{D}{(-1)\dfrac{z^{-1}}{1-z^{-1}} +}\frac{-(D+1)}{2+}\frac{D-1}{(-3)\dfrac{z^{-1}}{1-z^{-1}} +} \frac{-(D+2)}{2+}\cdots\frac{D-k+1}{(-2k+1)\dfrac{z^{-1}}{1-z^{-1}} +}\frac{-(D+k)}{2+}\cdots \tag{9}$$

$$G_q(z) = \alpha_0 + \frac{\eta_1}{\beta_1 z^{-1} +}\frac{\mu_1}{\alpha_1 +}\frac{\eta_2}{\beta_2 z^{-1} +}\frac{\mu_2}{\alpha_2 +}\cdots \frac{\eta_{N_r}}{\beta_{N_r} z^{-1} +}\frac{\mu_{N_r}}{\alpha_{N_r}}. \tag{10}$$

Fig. 2 shows the ladder structure of the filter, in which Fig. 2(a) is the main part of the ladder-shaped structure, and the specific structure of the ladder crossbar $G_{qN_r}(z)$ is shown in Fig. 2(b). The transfer function of this ladder-shaped structure is shown in (10).

Using the ladder structure of (10) to express z^{-D} in (9), that is, the substitution is as shown in (11), and the expression of z^{-D} at this time is as shown in (12).

$$\begin{cases} 1 \to \alpha_0 \\ (2, -2k+1) \to (\alpha_k, \beta_k)\ ,\ k \in [1, N_r] \\ (D-k+1, -D-k) \to (\eta_k, \mu_k)\ ,\ k \in [1, N_r] \\ \dfrac{z^{-1}}{1-z^{-1}} \to z^{-1} \end{cases} \tag{11}$$

$$z^{-D} = 1 + \frac{D}{-\dfrac{z^{-1}}{1-z^{-1}} +}\frac{-D-1}{2+}\frac{D-1}{-3\dfrac{z^{-1}}{1-z^{-1}} +}$$

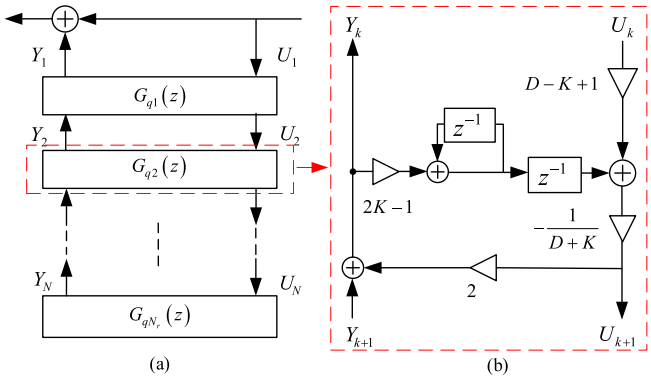

Fig. 3. Ladder structure of Thiran approximation IIR filter. (a) z^{-D} ladder structure main body. (b) Details in the bar.

$$\frac{-D-2}{2+}\cdots\frac{D-N_r+1}{(1-2N_r)\dfrac{z^{-1}}{1-z^{-1}}+}\frac{-D-N_r}{2}. \quad (12)$$

From (12), it can construct the ladder structure of the IIR filter using the Thiran approximation method [44], as shown in Fig. 3. In Fig. 3, the N_r-order filter has N_r ladders. Compared with the direct-form structure Thiran method, the ladder structure used in this article is simple and easy to calculate, and the adder and shift register in the digital circuit can realize the integer multiplication, so this method only needs two multipliers for each ladder to realize the function of each ladder, which simplifies the hardware implementation steps.

To enhance the stability of the system and ensure the resonance gain of the controller in the middle and low-frequency bands, Q selects the zero-phase-shift low-pass filter Qz in this article. To make the RC gain higher than the open-loop gain when Q is a constant with a value of 0.98 at 550 Hz, Qz chooses $Q(z)=0.15z+0.7+0.15z^{-1}$. Assuming that the grid-side frequency is 50 Hz, $N=200$ is an integer at this time. However, when the grid-side frequencies are 49.5 and 49.8 Hz, N is 202.02 and 200.8, respectively, and when the grid-side frequencies are 50.2 Hz and 50.5 Hz, N is 199.2 and 198.02, respectively. At the latter four frequencies, N is a fraction.

In view of the previous analysis, FD can be achieved through the Thiran digital filter, and the open-loop amplitude gain of FARC is as shown in Fig. 4. Fig. 4 shows that the designed FARC can effectively correct the controller gain when the fundamental resonant frequency is in the range of 49.5–50.5 Hz. Making the open-loop gain of the repetitive controller at the fundamental is always maintained at the highest gain (76.6 dB), and also can guarantee the steady-state error of the output current is minimized.

III. Improved FARC Strategy Design

A. Plant Modeling

In this article, the three-phase *LCL* grid-connected inverter is selected as the plant model. Fig. 5 depicts the structure of the control system used in the three-phase grid-connected inverter, where $V_{\rm dc}$ is the bus voltage, L_1 is the inverter side inductor, C is the filter capacitor, L_2 is the grid inductor, i_{abc} and i_{gabc} are

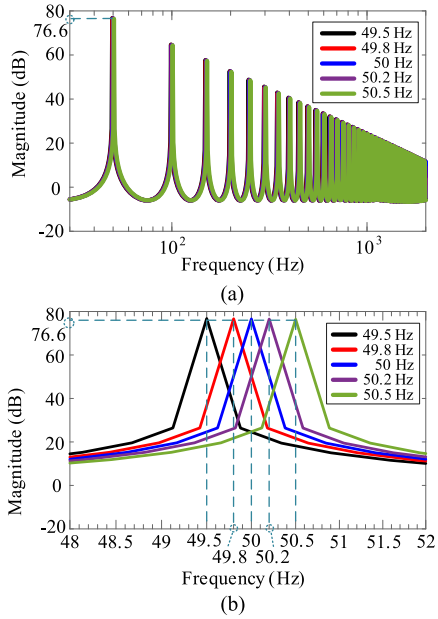

Fig. 4. FARC open loop amplitude gain. (a) Open-loop gain of FARC under grid-side frequency fluctuation. (b) Open-loop gain of FARC around the fundamental frequency.

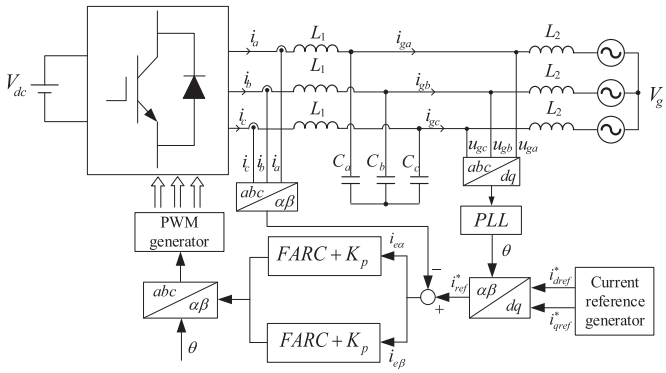

Fig. 5. Three-phase grid-connected inverter control system structure diagram.

the bridge side current and the grid current, and V_g is the grid voltage.

If i_{gabc} is chosen as the controlled variable, the controlled object is equivalent to a third-order system; furthermore, the system has a low stability margin, so this choice requires additional consideration of the system damping characteristics. From Fig. 5, i_{abc} is taken as the controlled quantity, at this time, the controlled object is equivalent to a first-order system, and the system stability margin is high. Moreover, the *LCL* third-order filter can achieve the harmonic suppression effect.

Under the condition that the dc bus voltage of the inverter is constant, the waveform quality control technology based on RC is used for the controlled variable, and the grid-connected inverter outputs a sine wave current with unity power factor and maintains a low total harmonic distortion (THD).

B. Boundary Conditions

Proportional controller is selected to combine the repetitive controller and the plug-in structure, which is shown in Fig. 1 and

the parallel structure has less influence on the gain of RC. Parallel RC can expand the value range of $K_{\rm rc}$, and the control structure in Fig. 1 can expand $K_{\rm rc}$ by K_p times on the original basis. However, from the point of view of system design, selecting the embedded control structure, $G_p(z)$ and $G_c(z)$ can be regarded as the same controlled object $P(z)$, and the form of $P(z)$ is as follows:

$$P(z) = \frac{G_c(z)G_p(z)}{1 + G_c(z)G_p(z)}. \tag{13}$$

According to (13), the structure of $P(z)$ is a closed-loop transfer function, and by designing K_p, $P(z)$ is corrected to close to 1 in the middle and low-frequency bands. By designing z^m of the repetitive controller to compensate for the system phase and each link independent, a better control effect can be obtained.

$G_{\rm rc}(z)$ is shown as

$$G_{\rm rc}(z) = \frac{Qz^{-N}}{1 - Qz^{-N}} z^m K_{\rm rc} S(z). \tag{14}$$

The error transfer function of the control structure shown in Fig. 1 is as follows:

$$E(z) = \frac{1}{1 + (1 + G_{\rm rc})\, G_c(z)G_p(z)} \cdot R(z) - \frac{1}{1 + (1 + G_{rc})\, G_c(z)G_p(z)} \cdot D(z). \tag{15}$$

Bringing (13) and (14) into (15), the error transfer function can be derived as

$$E(z) = \frac{\left(1 - Qz^{-N}\right)\left(1 - P(z)\right)}{1 - Qz^N\left[1 - z^m K_{\rm rc} S(z)P(z)\right]} \cdot R(z) - \frac{\left(1 - Qz^{-N}\right)\left(1 - P(z)\right)}{1 - Qz^N\left[1 - z^m K_{\rm rc} S(z)P(z)\right]} \cdot D(z). \tag{16}$$

A sufficient condition for the stability of the system is shown in (17), and meanwhile, the condition holds that roots of $1 + G_p(z)G_c(z) = 0$ are inside the unit circle.

$$|Q \cdot [1 - z^m K_{\rm rc} S(z)P(z)]| < 1,\ \forall z = e^{j\omega T_s},$$
$$0 < \omega < \frac{\pi}{T_s}. \tag{17}$$

C. Parameter Design

To improve the system stability margin and enhance the system attenuation capability in the high-frequency band, the cutoff frequency of the second-order low-pass filter $S(z)$ is selected as 550 Hz. After discretization, it is shown as follows:

$$S(z) = \frac{0.05061\, z + 0.04306}{z^2 - 1.523\, z + 0.6166}. \tag{18}$$

The transfer function from i_{abc} to u_{abc} is expressed as follows:

$$G_p(z) = \frac{L_2 C s^2 + 1}{L_1 L_2 C s^3 + (L_1 + L_2)s}. \tag{19}$$

By designing the proportional link, the middle- and low-frequency bands of the closed-loop Bode diagram after system correction realizes zero gain and zero-phase-shift, so $K_p = 3$ is selected.

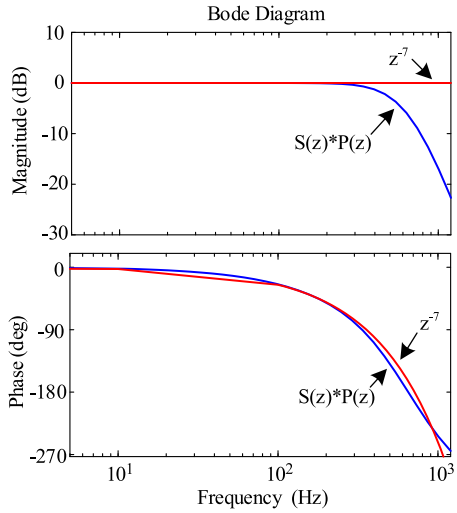

Fig. 6. Bode plot of $S(z)P(z)$ and compensation for advanced links z^{-m}.

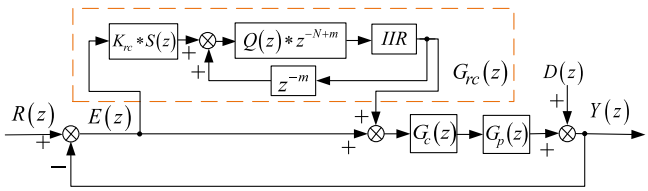

Fig. 7. FARC structure block diagram.

The advance compensation element z^m performs phase compensation on the $S(z)P(z)$ element. Fig. 6 shows that z^7 can perfectly cancel the phase delay of the $S(z)P(z)$ element up to 1000 Hz. Therefore, $m = 7$ is used for the advance compensation in the simulation. The difference is that in the actual experiment, due to the hardware circuit having its own delay, $m = 8$ is adopted. Analytical (13), $K_{\rm rc}$ affects the stability of the RC, and the $S(z) \cdot P(z) \cdot z^d$ link correction is close to 1.

The stable value range of the repetitive controller is shown as follows:

$$|Q - K_{\rm rc}| < 1. \tag{20}$$

Since the value of Q is close to 1, it can be obtained as follows:

$$0 < K_{\rm rc} < 2. \tag{21}$$

Taking the parameter variation and the stability margin in the practical application into account, the value of $K_{\rm rc}$ should reserve a certain margin. Due to the existence of a proportional link in the compound control, the RC forward gain loss by $K_{\rm rc}$ can be compensated by K_p, and $K_{\rm rc}$ is taken as 1 in this article.

From (17), the steady-state judgment formula of the system is obtained as follows:

$$|(1 - z^m K_{\rm rc} S(z)P(z)) \cdot Q \cdot \text{IIR}| < 1. \tag{22}$$

From (22), the design of $K_{\rm rc}$, Q, and z^m links is not affected by the IIR filter.

Fig. 7 is a block diagram of the FARC structure based on the IIR filter obtained on the basis of Fig. 1.

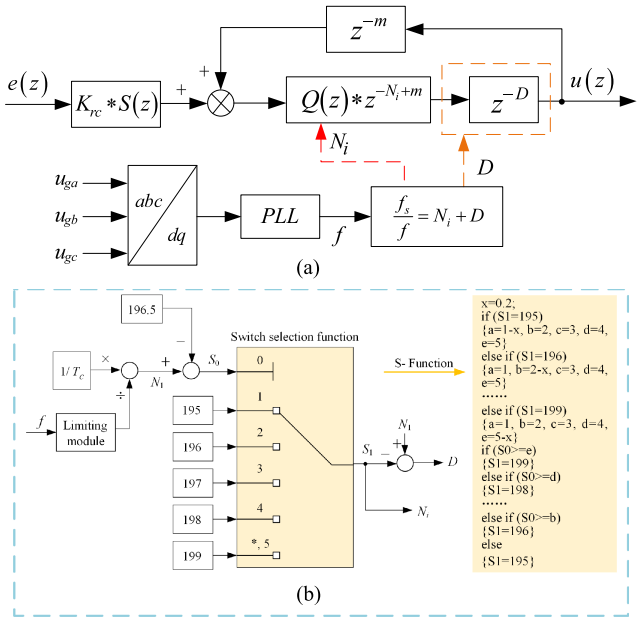

Fig. 8. FARC structure diagram. (a) Structure diagram of FARC. (b) Detailed implementation structure of FD module.

In this article, the sampling frequency is 10 kHz, the grid-side frequency of the three-phase grid-connected inverter RC strategy designed is 50 Hz, and the grid frequency fluctuation range is 49.5–50.5 Hz, corresponding to $N = N_i + D$. The effect of D falling in $[N_r - 0.5,\ N_r + 0.5]$ can be achieved by changing the value of N_i. Assume that the grid-side frequency is 49.6 Hz at a certain time, corresponding to $N = 200.8$, $N_r = 3$, $d = -0.2$, and $N_i = 198$ at this moment, assume which frequency is 50.4 Hz at a certain moment, corresponding to $N = 198.4$, $N_r = 3$, $d = 0.4$, and $N_i = 195$ at this time.

Fig. 8 shows the structure diagram of FARC applied to the three-phase grid-connected inverter, where the FD module in Fig. 8(a) is used to modify the IIR filter parameters in real time to achieve FARC, and Fig. 8(b) details the implementation process of the FD module. Since this article is conducted within the frequency range of 49.5–50.5 Hz, a limiting module with an upper limit of 50.5 Hz and a lower limit of 49.5 Hz is added after obtaining the grid frequency. After that, the corresponding values of N_i and D are obtained through the switch selection module. To prevent frequent switching of internal mode, the hysteresis function is incorporated into the switch. Fig. 9 shows the structural details of z^{-D} in the FARC internal model.

IV. Experimental Verifications

A. Test-Rig Description

To demonstrate the above analysis and the effectiveness of the FARC algorithm based on the ladder structure Thiran filter proposed in this article, a simulation model of a three-phase *LCL* inverter is established using the MATLAB/Simulink software. Fig. 10 shows the system topology of the experimental platform, and Fig.11 displays the experimental setup of the three-phase grid-connected system.

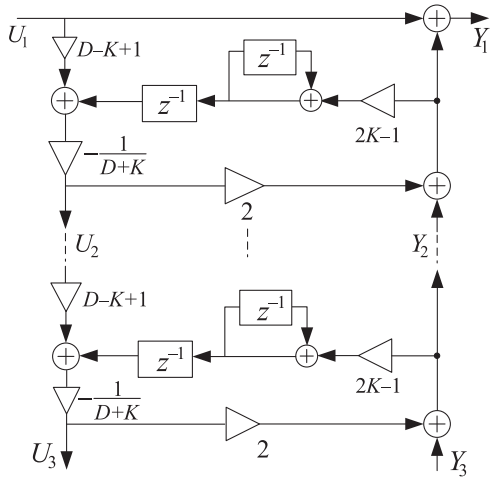

Fig. 9. Structure details of z^{-D} in the FARC internal model.

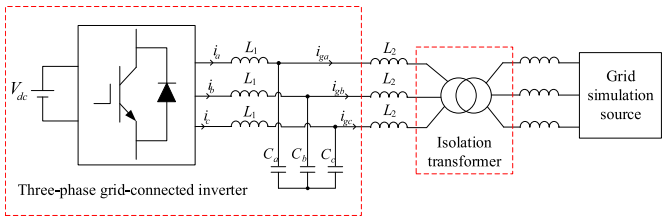

Fig. 10. Experimental platform system topology.

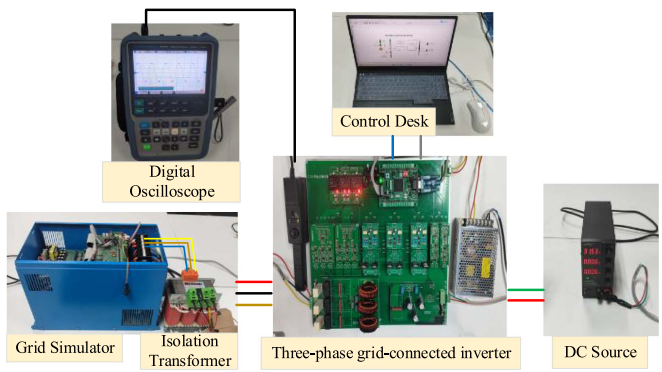

Fig. 11. Experimental setup of a three-phase grid-connected system.

The experimental setup concludes with a 300-W three-phase *LC* grid-connected inverter platform, a grid simulator, an isolation transformer, an auxiliary power, a dc source, a digital oscilloscope, and a control desk. Among them, the grid simulator is used to simulate the change in grid frequency. The inverter platform is powered by the auxiliary power, as well as the dc side of the inverter is connected to the dc source, and the ac side is connected to the power grid simulator through the isolation transformer. In addition, the grid-side leakage inductance of the isolation transformer is treated as the grid-side inductance of the inverter to realize the corresponding relationship between the experimental model and the simulation model.

TABLE I
MAIN PARAMETERS OF THE INVERTER

Parameter	Value
Switching frequency	10 kHz
Sampling period T_s	0.1 ms
Grid frequency f_g	49.5–50.5 Hz
Inverter side inductor L_1	2 mH
Transformer leakage inductance L_2	0.073 mH
Filter capacitor C (triangular wiring)	1 μF
DC-link voltage V_{dc}	30 V
Grid voltage RMS V_g	12 V
Reference current amplitude	4 A
stability coefficient Qc	0.95
stability coefficient Qz	$0.15z+0.7+0.15z^{-1}$
The low-pass filtering part $S(z)$	$\frac{0.05061z+0.04306}{z^2-1.523z+0.6166}$

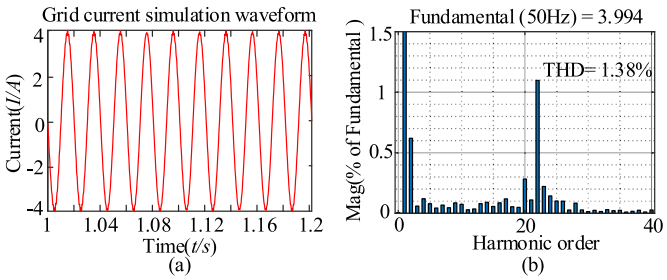

Fig. 12. Simulation analysis results of grid-connected current of Q_cRC when grid frequency is 50 Hz. (a) Grid current. (b) Spectrum of the grid current.

This article selects the following three control strategies for comparison:

1) RC using the constant stability factor Q_c (Q_cRC);
2) RC using the low-pass filter Q_z (Q_zRC);
3) on the basis of Q_zRC, the RC introducing the ladder structure Thiran method IIR filter (FARC).

The grid-connected experiments are carried out under three working conditions when grid voltage frequencies are 49.5, 50, and 50.5 Hz, and the control accuracy and harmonic content of grid-connected current are analyzed. In addition, after the actual power grid frequency fluctuates, it will stabilize at about 50 Hz, therefore, by analyzing and comparing the grid-tied current fundamental amplitude and waveform quality at different frequencies, the frequency immunity of different RC algorithms can be measured. The main parameters of the inverter are shown in Table I.

B. Simulation Research

In the case when the grid frequency is 50 Hz, the simulation results of the three strategies are shown in Figs. 12–14. It can be seen from this that when the reference grid-side current amplitude is 4 A, the grid current fundamental amplitudes of the three control strategies are 3.994 A, 3.992 A, and 3.992 A,

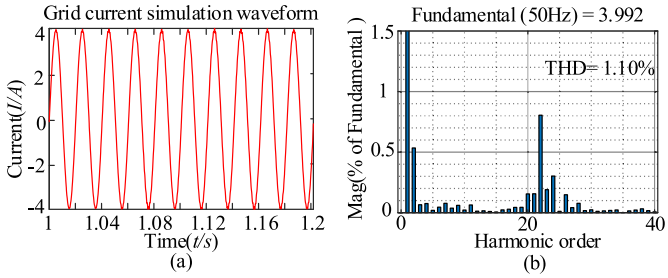

Fig. 13. Simulation analysis results of grid-connected current of Q_zRC when grid frequency is 50 Hz. (a) Grid current. (b) Spectrum of the grid current.

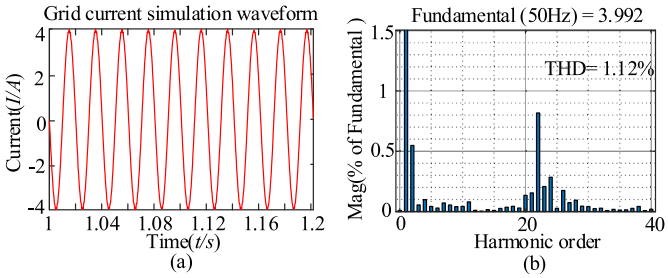

Fig. 14. Simulation analysis results of grid-connected current of FARC when grid frequency is 50 Hz. (a) Grid current. (b) Spectrum of the grid current.

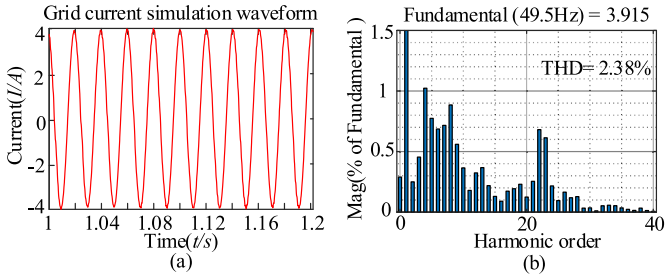

Fig. 15. Simulation analysis results of grid-connected current of Q_cRC when grid frequency is 49.5 Hz. (a) Grid current. (b) Spectrum of the grid current.

respectively. The corresponding amplitude error is 0.15%, 0.2%, and 0.2%. The THD of the output current is 1.38%, 1.10%, and 1.12%, respectively.

In addition, the following information can be obtained from the grid-connected current spectrum. Compared with Q_cRC, Q_zRC and FARC have a certain degree of reduction in the frequency of the 20th to 25th harmonic components, and the three strategies have good control effects at 50 Hz. The analysis shows that the three control strategies all have high current tracking ability at 50 Hz and meet the requirements of grid-connected harmonic content so that the system can be kept stable.

It has been verified that the grid current tracking accuracy and THD of the three schemes at the fundamental frequency are the same. However, according to theoretical analysis, the grid current tracking accuracy and THD of the three schemes will be different when the grid frequency fluctuates.

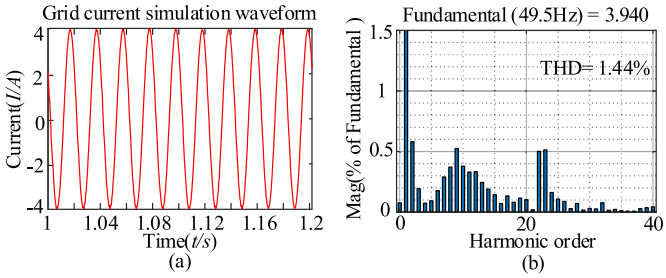

Fig. 16. Simulation analysis results of grid-connected current of Q_zRC when grid frequency is 49.5 Hz. (a) Grid current. (b) Spectrum of the grid current.

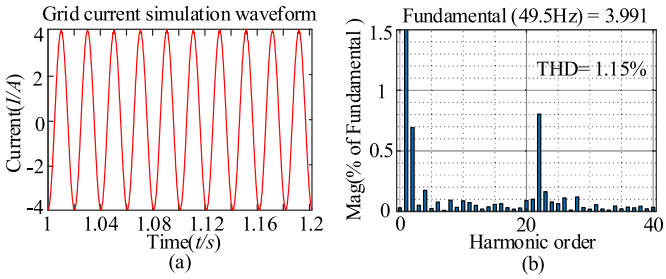

Fig. 17. Simulation analysis results of grid-connected current of FARC when grid frequency is 49.5 Hz. (a) Grid current. (b) Spectrum of the grid current.

In the case when the grid frequency is 49.5 Hz, $N = 202.02$ is a fraction. Under this condition, Figs. 15–17 show the fundamental frequency amplitude and THD of the three schemes. Among them, Fig. 15 shows that the fundamental amplitude of the Q_cRC at 49.5 Hz is 3.915 A, the THD is 2.38%, and the corresponding amplitude error is 2.125%. Fig. 16 shows that the fundamental amplitude of Q_zRC is 3.940 A, the THD is 1.44%, and the corresponding amplitude error is 1.5%. Fig. 17 shows that the fundamental amplitude of the FARC scheme proposed in this article is 3.991 A, the THD is 1.15%, and the corresponding amplitude error is 0.225%.

As can be seen from Figs. 15–17 that compared with Q_cRC, the amplitude tracking effect of Q_zRC is improved, and the THD is also decreased, but the amplitude error is still large.

Compared with the first two methods, the grid current tracking effect of FARC is enhanced. Moreover, the amplitude error is very close to the amplitude error at 50 Hz. In Addition, it can be obtained from the grid-connected current spectrum that the THD of FARC is also relatively low, and the low-frequency suppression effect of FARC is remarkable.

In the case when the grid frequency is 50.5 Hz, $N = 198.02$ is a fraction. Figs. 18–20 show the fundamental frequency amplitude and THD of the three schemes under this condition. As shown in Figs. 18–20, the THDs of Q_cRC, Q_zRC, and FARC at 50.5 Hz are 2.45%, 1.46%, and 1.32%, respectively, the fundamental amplitudes are 4.072 A, 4.045 A, and 3.989 A, respectively, and the corresponding amplitudes errors are 1.8%, 1.125%, and 0.275%, respectively.

It can be seen from the above data that, similar to the simulation results at 49.5Hz, compared with Q_cRC, the amplitude tracking ability of Q_zRC is enhanced at 50.5 Hz, and the THD

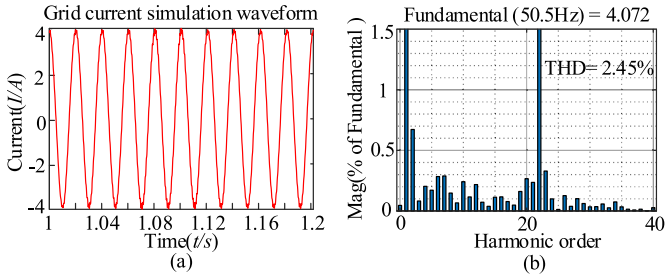

Fig. 18. Simulation analysis results of grid-connected current of Q_cRC when grid frequency is 50.5 Hz. (a) Grid current. (b) Spectrum of the grid current.

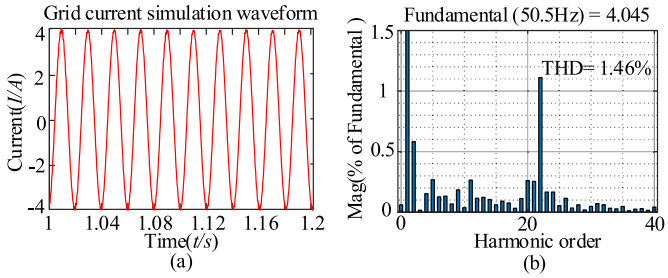

Fig. 19. Simulation analysis results of grid-connected current of Q_zRC when grid frequency is 50.5 Hz. (a) Grid current. (b) Spectrum of the grid current.

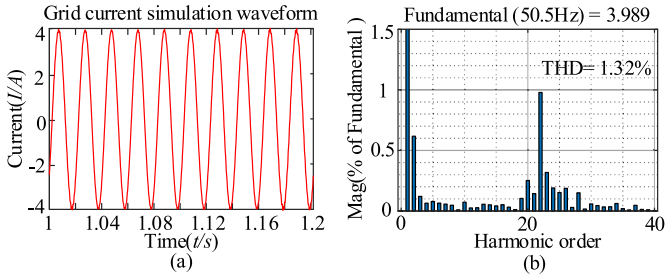

Fig. 20. Simulation analysis results of grid-connected current of FARC when grid frequency is 50.5 Hz. (a) Grid current. (b) Spectrum of the grid current.

is reduced to less than 1.5%, but the amplitude error is still greater than 1%. On the basis of Q_zRC, the THD of FARC is further reduced, the grid current tracking effect of FARC is further enhanced, and the amplitude error is reduced below 0.3%. Furthermore, it can be seen from the grid current spectrum that compared with Q_cRC, FARC has a significant inhibitory effect on the 22nd harmonic component.

As can be seen from the simulation results at 49.5 and 50.5 Hz, when the grid frequency fluctuates, the harmonic content of the Q_zRC is suppressed compared to Q_cRC. However, the introduction of the Q value reduced the fundamental frequency gain, so that the amplitude gain of Q_zRC is still relatively high, which cannot meet the high tracking accuracy requirements of the grid-connected current. On the basis of Q_zRC, the magnitude gains of the FARC strategy proposed in this article are further improved, and the suppression effect on the low-order harmonics of the grid-connected current is also very good. Moreover, the

TABLE II
SIMULATED GRID-CONNECTED CURRENT AND FUNDAMENTAL AMPLITUDE OF THREE MODES

Algorithm	*f*/Hz	THD/%	Fundamental amplitude/A	Tracking precision error/%
	49.5	2.38	3.915	2.125
Q_cRC	50	1.38	3.994	0.15
	50.5	2.45	4.072	1.8
	49.5	1.44	3.940	1.5
Q_ZRC	50	1.10	3.992	0.2
	50.5	1.46	4.045	1.125
	49.5	1.15	3.991	0.225
FARC	50	1.12	3.992	0.2
	50.5	1.32	3.989	0.275

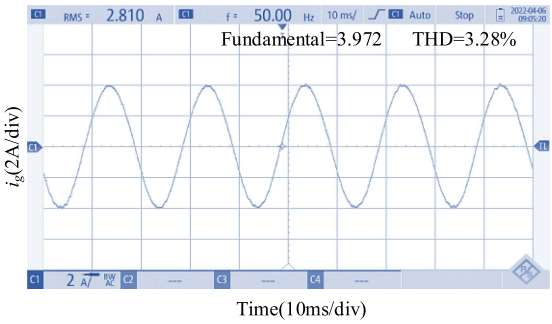

Fig. 21. Experimental waveform of grid-connected current of Q_cRC when grid frequency is 50 Hz.

THD and grid current tracking accuracy meet the grid-connected requirements.

The grid-connected current performance comparison of the three modes under the three working conditions is shown in Table II. The following information can be obtained from Table II. At 50 Hz, the three algorithms can maintain high control accuracy and harmonic suppression capability. In the case of grid-side frequency fluctuations, the control accuracy of Q_cRC and Q_zRC is greatly affected, and the grid current accuracy error of the two strategies exceeds 1%, whereas the accuracy of FARC in this article is not affected, and the current error accuracy is always within 0.3%. Simulation shows that the proposed FARC strategy based on the improved IIR filter can maintain a constant high gain at any frequency, thus ensuring high tracking accuracy and low grid-connected current THD, proving the effectiveness of the strategy.

C. Experimental Results

It can be obtained from the above simulation phenomenon and result analysis that theoretically the Q_cRC cannot maintain a high open-loop gain near the fundamental frequency, so the current tracking effect will be poor in the case of frequency fluctuations. Figs. 21–23 show the grid-connected current waveform, fundamental frequency amplitude, and THD of the Q_cRC at 50 Hz, 49.5 Hz, and 50.5 Hz, respectively. Among them, the grid simulator is used to generate three-phase ac voltages of various frequencies.

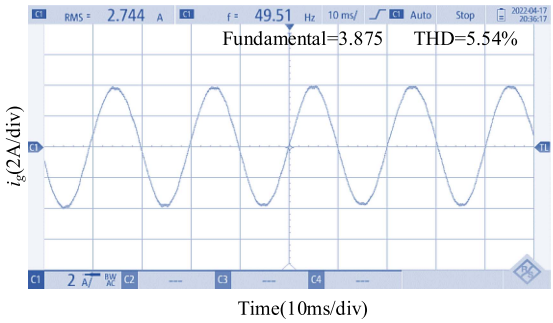

Fig. 22. Experimental waveform of grid-connected current of Q_cRC when grid frequency is 49.5 Hz.

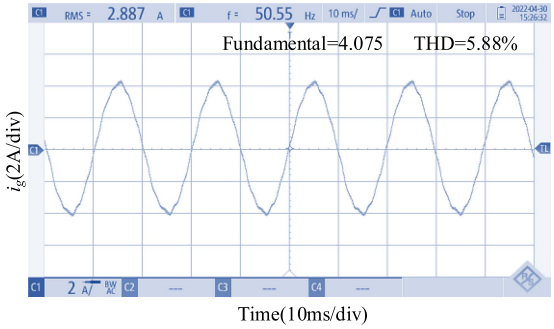

Fig. 23. Experimental waveform of grid-connected current of Q_cRC when grid frequency is 50.5 Hz.

As shown in Fig. 21, when the grid-side frequency is 50 Hz, the fundamental amplitude of the Q_cRC is 3.972 A after fast Fourier transform (FFT) analysis, and the amplitude error is 0.7%, besides the THD is 3.28%, which is less than 5%, meeting the THD standard value of the grid-connected experiment. From these phenomena can be seen, the grid current tracking effect and THD are both very good for Q_cRC at 50 Hz, which are consistent with the theoretical analysis results and simulation results.

Figs. 22 and 23 show the case of Q_cRC at 49.5 Hz and 50.5 Hz, respectively. From them, the following information can be obtained. At 49.5 Hz, according to FFT analysis, the fundamental amplitude of the grid-connected current is 3.875 A, the THD is 5.54%, and the calculated amplitude error is 3.125%. Similarly, at 50.5 Hz, the fundamental amplitude of the grid-connected current is 4.075 A, the error is 1.875%, and the THD is 5.88%. The experimental results show that the amplitude error and THD of Q_cRC at 49.5 and 50.5 Hz are much higher than that of 50 Hz, and the THD at two frequencies is greater than the grid-connected THD standard.

It can be concluded that, at the frequency change, Q_cRC neither guarantees the high tracking accuracy of grid-connected current nor meets the requirements of grid-connected harmonic content.

As described in the theoretical analysis of this article, in the light of the problem of poor control effect of Q_cRC at

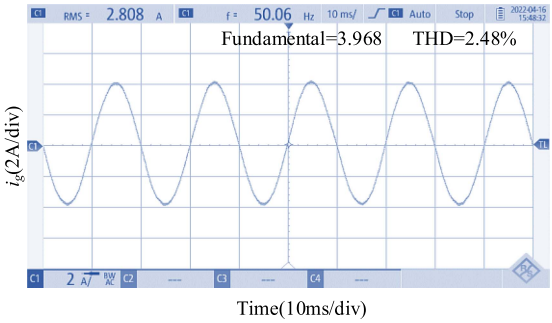

Fig. 24. Experimental waveform of grid-connected current of Q_zRC when grid frequency is 50 Hz.

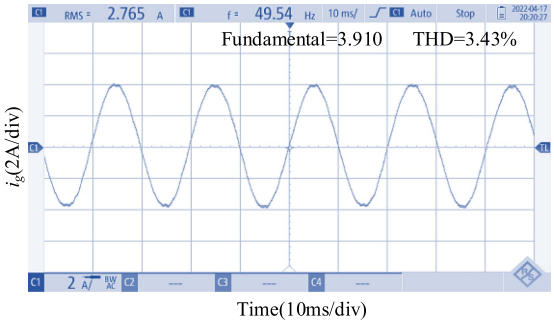

Fig. 25. Experimental waveform of grid-connected current of Q_zRC when grid frequency is 49.5 Hz.

the frequency fluctuations, the stability coefficient Q_z can be introduced in the internal model to improve this problem. In view of this, this article introduces Q_z as the comparison strategy, that is, Q_zRC. From the simulation result, consistent with the theoretical analysis, Q_zRC can improve the tracking accuracy and reduce the THD at a certain.

Fig. 24 shows the experimental results of Q_zRC at the grid frequency of 50 Hz. The results show that the fundamental amplitude of the grid-connected current of Q_zRC at 50 Hz is 3.968 A, the error is 0.8%, and the harmonic content THD is 2.48%. These data are very close to the data of Q_cRC at 50 Hz, that is, the control effect of Q_zRC and Q_cRC at the fundamental frequency is similar, which is consistent with the simulation.

When the grid frequency is 49.5 and 50.5 Hz, as shown in Figs. 25 and 26, the control effect of Q_zRC is as follows: the grid current THD is 3.43% and 3.50%, the fundamental frequency amplitudes are 3.910 and 4.034 A, and the tracking errors are 2.25% and 0.85%, respectively. It can be seen that the amplitude tracking effect of Q_zRC fluctuates greatly when the frequency changes and the harmonic suppression ability is weakened. Despite these two frequencies, the THD meets the grid-connection requirements below 5%, it is still larger than the THD at the fundamental frequency. Compared with Q_cRC, the amplitude error and the THD of Q_zRC are reduced, and the grid current tracking effect is enhanced, but the fundamental gain of the power grid is also attenuated due to the introduction of Q_z, which is the same conclusion as the simulation results.

From the above experimental analysis results, the harmonic content of Q_zRC near the fundamental frequency is suppressed

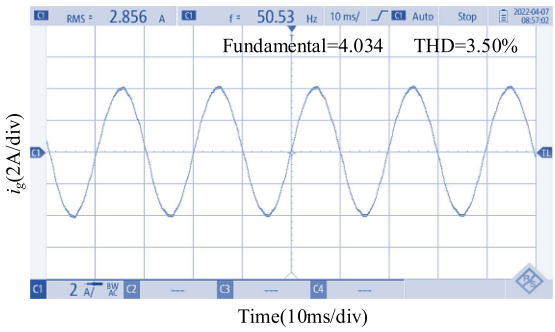

Fig. 26. Experimental waveform of grid-connected current of Q_zRC when grid frequency is 50.5 Hz.

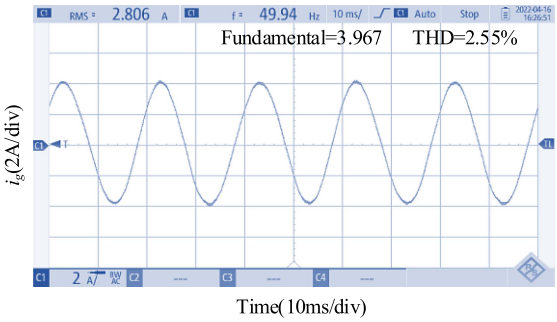

Fig. 27. Experimental waveform of grid-connected current of FARC when grid frequency is 50 Hz.

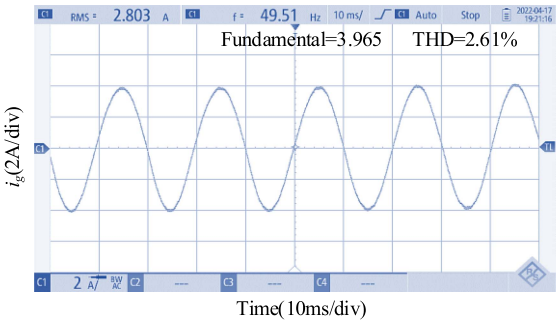

Fig. 28. Experimental waveform of grid-connected current of FARC when grid frequency is 49.5 Hz.

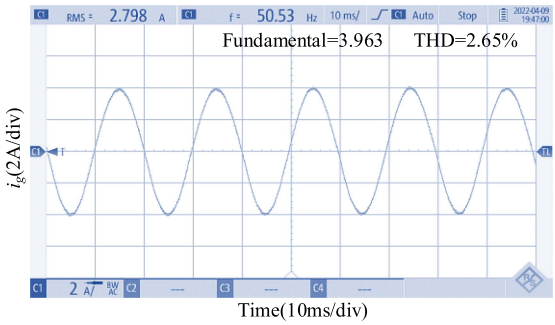

Fig. 29. Experimental waveform of grid-connected current of FARC when grid frequency is 50.5 Hz.

TABLE III
EXPERIMENT GRID-CONNECTED CURRENT AND FUNDAMENTAL AMPLITUDE OF THREE MODES

Algorithm	f/Hz	THD/%	Fundamental amplitude/A	Tracking precision error/%
	49.5	5.54	3.875	3.125
Q_cRC	50	3.28	3.972	0.7
	50.5	5.88	4.075	1.875
	49.5	3.43	3.910	2.25
Q_zRC	50	2.48	3.968	0.8
	50.5	3.50	4.034	0.85
	49.5	2.61	3.965	0.875
FARC	50	2.55	3.967	0.825
	50.5	2.65	3.963	0.925

to a certain extent compared with Q_cRC, but the gain still cannot meet the high tracking accuracy of grid-connected current. To solve the problem of insufficient fundamental gain when the grid frequency fluctuates, on the basis of Q_zRC, a Thiran filter with a ladder structure is introduced to construct the FARC. The experiment results are shown in Figs. 27–29.

In the case of a grid frequency is 50 Hz, the experimental waveform of the grid-connected current of FARC is shown in Fig. 27. The grid current fundamental amplitude is 3.966 A, the error is 0.85%, and the THD value is 2.58%. The results display that the introduced ladder structure does not affect the fundamental frequency gain at 50 Hz, and the THD is also relatively low.

As shown in Figs. 28 and 29, the experimental data for FARC at 49.5 and 50.5 Hz are as follows: the fundamental wave amplitudes are 3.965 and 3.960 A, the THD values are stable at 2.68% and 2.59%, and the amplitude error is within 1%. The grid current tracking accuracy and harmonic suppression ability are consistent with the fundamental frequency, which proves that FARC can well adapt to the grid frequency fluctuations.

The grid-connected current performance comparison of the three modes under the three working conditions is shown in Table III. From Table III, it can be seen that at 50 Hz, the three algorithms can maintain high control accuracy and harmonic suppression capability when actually connected to the grid. However, in the case of grid-side frequency fluctuations, the control accuracy of Q_cRC and Q_zRC is greatly affected, so that the current accuracy error exceeds 1%, and the control accuracy of FARC is not affected by the frequency fluctuation on the grid-side, moreover, the current error accuracy is always within 1%.

From the simulation and experimental analysis, it can be concluded that under the change of power grid frequency, the FARC algorithm after introducing the ladder structure Thiran filter is better than Q_cRC and Q_zRC in terms of tracking accuracy and control effect, and the FARC proposed in this article is easy to implement. Furthermore, it can effectively correct the resonant peak frequency of the repetitive controller, ensure the tracking control effect of the grid-connected current, and realize the frequency adaptation of RC.

V. CONCLUSION

In this article, an FARC based on an improved IIR filter is designed. A new ladder structure is introduced in the RC internal model, which simplifies the structure of the IIR filter and realizes the frequency adaptation. On the experimental platform of the three-phase grid-connected inverter, the amplitudes of THD and a fundamental wave of grid-connected currents under three control strategies at different frequencies are compared. From the analysis, it can be seen that the FARC based on the improved IIR filter proposed in this article effectively corrects the resonant gain range of the RC and can ensure the tracking control effect of the grid-connected current when the frequency is changed and verify the effectiveness and accuracy of the improved FARC.

APPENDIX

The derivation process of (32) is as follows.

From [42, Appendix II], we can see that the continuous expansion of $(1+x)^k$ proposed by Lagrange in 1776 is

$$(1+x)^k = \cfrac{1}{1-\cfrac{kx}{1+\cfrac{\frac{1\cdot(1+k)}{1\cdot 2}x}{1+\cfrac{\frac{1\cdot(1-k)}{2\cdot 3}x}{1+\cfrac{\frac{2\cdot(2+k)}{3\cdot 4}x}{1+\cfrac{\frac{2\cdot(2-k)}{4\cdot 5}x}{1+\cfrac{\frac{3\cdot(3+k)}{5\cdot 6}x}{1+\ddots}}}}}}}. \tag{23}$$

For easy observation, (23) can be abbreviated to the following form:

$$(1+x)^k = \frac{1}{1-}\frac{kx}{1+}\frac{\frac{1\cdot(1+k)}{1\cdot 2}x}{1+}\frac{\frac{1\cdot(1-k)}{2\cdot 3}x}{1+}\frac{\frac{2\cdot(2+k)}{3\cdot 4}x}{1+}\frac{\frac{2\cdot(2-k)}{4\cdot 5}x}{1+}\frac{\frac{3\cdot(3+k)}{5\cdot 6}x}{1+}\cdots. \tag{24}$$

Performing the substitution $k \leftarrow y$ on (24) yields $(1+x)^y$ as

$$\begin{aligned}(1+x)^y &= \frac{1}{1-}\frac{yx}{1+}\frac{\frac{(1+y)}{2}x}{1+}\frac{\frac{(1-y)}{6}x}{1+}\frac{\frac{(2+y)}{6}x}{1+}\cdots \\ &= \frac{1}{1-}\frac{yx}{1+}\frac{(1+y)x}{2+}\frac{(1-y)x}{3+}\frac{(2+y)x}{2+}\cdots.\end{aligned} \tag{25}$$

From the continuous fraction theorem on [43, page 19], we can obtain

$$f_n = b_0 + \frac{c_1a_1}{c_1b_1+}\frac{c_1c_2a_2}{c_2b_2+}\frac{c_2c_3a_3}{c_3b_3+}\cdots\frac{c_{n-1}c_na_n}{c_nb_n+},\ n \geq 0. \tag{26}$$

To make the molecule free of x, we can use the theorem of the continuous fraction [as shown in (26)] to get the following

equation:

$$(1+x)^y = \frac{1}{1-}\frac{y}{\frac{1}{x}+}\frac{1+y}{2+}\frac{1-y}{\frac{3}{x}+}\frac{2+y}{2+}\frac{2-y}{\frac{5}{x}+}\frac{3+y}{2+}\cdots. \tag{27}$$

Using the characteristics of continuous fractions, we have

$$\begin{aligned}(1+x)^y &= \frac{1}{\frac{1}{(1+x)^y}} = \frac{1}{\left(\frac{1}{1+x}\right)^y} \\ &= \frac{1}{\left(1+\frac{-x}{1+x}\right)^y} = \left(1+\frac{-x}{1+x}\right)^{-y}.\end{aligned} \tag{28}$$

Performing the substitution $x \leftarrow (-x)/(1+x)\ ,\ y \leftarrow (-y)$ on (27) can get the following equation:

$$\begin{aligned}(1+x)^y &= \left(1+\frac{-x}{1+x}\right)^{-y} \\ &= \frac{1}{1-}\frac{-y}{-\frac{1+x}{x}+}\frac{1-y}{2+}\frac{1+y}{(-3)\frac{1+x}{x}+}\frac{2-y}{2+}\cdots.\end{aligned} \tag{29}$$

Performing the substitution $x \leftarrow x-1$ on (29), we have

$$x^y = \frac{1}{1-}\frac{-y}{-\frac{x}{x-1}+}\frac{1-y}{2+}\frac{1+y}{(-3)\frac{x}{x-1}+}\frac{2-y}{2+}\cdots. \tag{30}$$

Take the reciprocal of (30), which can be further simplified as

$$\begin{aligned}x^{-y} &= 1-\frac{-y}{-\frac{x}{x-1}+}\frac{1-y}{2+}\frac{1+y}{(-3)\frac{x}{x-1}+}\frac{2-y}{2+}\cdots \\ &= 1-\frac{y}{\frac{x}{x-1}+}\frac{y-1}{2+}\frac{-(1+y)}{\frac{3x}{x-1}+}\frac{y-2}{2+}\cdots \\ &= 1-\frac{y}{\frac{x}{x-1}+}\frac{y-1}{2-}\frac{1+y}{\frac{3x}{x-1}+}\frac{y-2}{2-}\cdots.\end{aligned} \tag{31}$$

Letting $x = z^{-1}$ and $y = -D$ on (31), z^{-D} is shown as

$$\begin{aligned}z^{-D} &= 1-\frac{-D}{\frac{z^{-1}}{z^{-1}-1}+}\frac{-(1+D)}{2-}\frac{1-D}{3\frac{z^{-1}}{z^{-1}-1}+}\frac{-(2+D)}{2-}\cdots \\ &= 1+\frac{D}{(-1)\frac{z^{-1}}{1-z^{-1}}+}\frac{-(1+D)}{2+}\frac{D-1}{(-3)\frac{z^{-1}}{1-z^{-1}}+} \\ &\quad \frac{-(2+D)}{2+}\cdots.\end{aligned} \tag{32}$$

REFERENCES

[1] Y. Yang, K. Zhou, H. Wang, and F. Blaabjerg, "Analysis and mitigation of dead-time harmonics in the single-phase full-bridge PWM converter with repetitive controllers," *IEEE Trans. Ind. Appl.*, vol. 54, no. 5, pp. 5343–5354, Sep./Oct. 2018.

[2] H. Zhang, X. Ruan, Z. Lin, L. Wu, Y. Ding, and Y. Guo, "Capacitor voltage full feedback scheme for LCL-type grid-connected inverter to suppress current distortion due to grid voltage harmonics," *IEEE Trans. Power Electron.*, vol. 36, no. 3, pp. 2996–3006, Mar. 2021.

[3] M. A. Herrán, J. R. Fischer, S. A. González, M. G. Judewicz, I. Carugati, and D. O. Carrica, "Repetitive control with adaptive sampling frequency for wind power generation systems," *IEEE J. Emerg. Sel. Topics Power Electron.*, vol. 2, no. 1, pp. 58–69, Mar. 2014.

[4] W. Jiang, X. Ding, Y. Ni, J. Wang, L. Wang, and W. Ma, "An improved deadbeat control for a three-phase three-line active power filter with current-tracking error compensation," *IEEE Trans. Power Electron.*, vol. 33, no. 3, pp. 2061–2072, Mar. 2018.

[5] F. Gonzalez-Espin, G. Garcera, I. Patrao, and E. Figueres, "An adaptive control system for three-phase photovoltaic inverters working in a polluted and variable frequency electric grid," *IEEE Trans. Power Electron.*, vol. 27, no. 10, pp. 4248–4261, Oct. 2012.

[6] B. Han, S. W. Jo, M. Kim, N. A. Dung, and J. S. Lai, "Improved odd-harmonic repetitive control scheme for Ćuk-derived inverter," *IEEE Trans. Power Electron.*, vol. 37, no. 2, pp. 1496–1508, Feb. 2022.

[7] P. Schulting, C. H. Broeck, and R. W. de Doncker, "Analysis and design of repetitive controllers for applications in distorted distribution grids," *IEEE Trans. Power Electron.*, vol. 34, no. 1, pp. 996–1004, Jan. 2019.

[8] Z. Liu, B. Zhang, K. Zhou, and J. Wang, "Virtual variable sampling discrete Fourier transform based selective odd-order harmonic repetitive control of DC/AC converters," *IEEE Trans. Power Electron.*, vol. 33, no. 7, pp. 6444–6452, Jul. 2018.

[9] Z. Liu, K. Zhou, Y. Yang, J. Wang, and B. Zhang, "Frequency adaptive virtual variable sampling-based selective harmonic repetitive control of power inverters," *IEEE Trans. Ind. Electron.*, vol. 68, no. 11, pp. 11339–11347, Nov. 2021.

[10] G. Pandove and M. Singh, "Robust repetitive control design for a three-phase four wire shunt active power filter," *IEEE Trans. Ind. Inform.*, vol. 15, no. 5, pp. 2810–2818, May 2019.

[11] H. Geng, Z. Zheng, T. Zou, B. Chu, and A. Chandra, "Fast repetitive control with harmonic correction loops for shunt active power filter applied in weak grid," *IEEE Trans. Ind. Appl.*, vol. 55, no. 3, pp. 3198–3206, May/Jun. 2019.

[12] C. Wu, H. Nian, B. Pang, and P. Cheng, "Adaptive repetitive control of DFIG-DC system considering stator frequency variation," *IEEE Trans. Power Electron.*, vol. 34, no. 4, pp. 3302–3312, Apr. 2019.

[13] M. Tang, A. Gaeta, A. Formentini, and P. Zanchetta, "A fractional delay variable frequency repetitive control for torque ripple reduction in PMSMs," *IEEE Trans. Ind. Appl.*, vol. 53, no. 6, pp. 5553–5562, Nov./Dec. 2017.

[14] M. Zhang, L. Huang, W. Yao, and Z. Lu, "Circulating harmonic current elimination of a CPS-PWM-based modular multilevel converter with a plug-in repetitive controller," *IEEE Trans. Power Electron.*, vol. 29, no. 4, pp. 2083–2097, Apr. 2014.

[15] Z. Liu, B. Zhang, K. Zhou, Y. Yang, and J. Wang, "Virtual variable sampling repetitive control of single-phase DC/AC PWM converters," *IEEE J. Emerg. Sel. Topics Power Electron.*, vol. 7, no. 3, pp. 1837–1845, Sep. 2019.

[16] Z.-X. Zou, K. Zhou, Z. Wang, and M. Cheng, "Frequency-adaptive fractional-order repetitive control of shunt active power filters," *IEEE Trans. Ind. Electron.*, vol. 62, no. 3, pp. 1659–1668, Mar. 2015.

[17] M. Zhu, Y. Ye, Y. Xiong, and Q. Zhao, "Multi-bandwidth repetitive control resisting frequency variation in grid-tied inverters," *IEEE J. Emerg. Sel. Topics Power Electron.*, vol. 10, no. 1, pp. 446–454, Feb. 2022.

[18] G. Escobar, G. A. Catzin-Contreras, and M. J. Lopez-Sanchez, "Compensation of variable fractional delays in the $6k\pm1$ repetitive controller," *IEEE Trans. Ind. Electron.*, vol. 62, no. 10, pp. 6448–6456, Oct. 2015.

[19] D. Chen, J. Zhang, and Z. Qian, "An improved repetitive control scheme for grid-connected inverter with frequency-adaptive capability," *IEEE Trans. Ind. Electron.*, vol. 60, no. 2, pp. 814–823, Feb. 2013.

[20] B. Han, J.-S. Lai, and M. Kim, "Down-sampled repetitive controller for grid-connected Ćuk CCM inverter," *IEEE J. Emerg. Sel. Topics Power Electron.*, vol. 10, no. 1, pp. 1125–1137, Feb. 2022.

[21] H. Lin, X. Guo, D. Chen, S. Wu, and G. Chen, "A frequency adaptive repetitive control for active power filter with 380V/75A SiC-inverter," *IEEE Trans. Ind. Appl.*, vol. 58, no. 4, pp. 5469–5479, Jul./Aug. 2022.

[22] J. Chen, H. Shao, and C. Liu, "An improved deadbeat control strategy based on repetitive prediction against grid frequency fluctuation for active power filter," *IEEE Access*, vol. 9, pp. 24646–24657, 2021.

[23] A. Zeineddine, A. Nafkha, S. Paquelet, C. Moy, and P. Y. Jezequel, "Comprehensive survey of FIR-based sample rate conversion," *J. Signal Process. Syst.*, vol. 93, pp. 113–125, 2021.

[24] Q. Zhao and Y. Ye, "Fractional phase lead compensation RC for an inverter: Analysis, design, and verification," *IEEE Trans. Ind. Electron.*, vol. 64, no. 4, pp. 3127–3136, Apr. 2017.
[25] Y. Yang, K. Zhou, H. Wang, F. Blaabjerg, D. Wang, and B. Zhang, "Frequency adaptive selective harmonic control for grid-connected inverters," *IEEE Trans. Power Electron.*, vol. 30, no. 7, pp. 3912–3924, Jul. 2015.
[26] L. Li, Z. Chen, S. S. Aphale, and L. Zhu, "Fractional repetitive control of nanopositioning stages for high-speed scanning using low-pass FIR variable fractional delay filter," *IEEE/ASME Trans. Mechatronics*, vol. 25, no. 2, pp. 547–557, Apr. 2020.
[27] Y. Yang, K. Zhou, and F. Blaabjerg, "Enhancing the frequency adaptability of periodic current controllers with a fixed sampling rate for grid-connected power converters," *IEEE Trans. Power Electron.*, vol. 31, no. 10, pp. 7273–7285, Oct. 2016.
[28] W. Wang, W. Lu, K. Zhou, and Q. Fan, "Fractional-order new generation of nk ± m-order harmonic repetitive control for PWM converters," *IEEE Access*, vol. 8, pp. 180706–180721, 2020.
[29] C. Zeng, S. Li, H. Wang, and H. Miao, "A fractional phase compensation scheme of PRMRC for LCL inverter connected to weak grid," *IEEE Access*, vol. 9, pp. 167027–167038, 2021.
[30] Z. Liu, B. Zhang, and K. Zhou, "Universal fractional-order design of linear phase lead compensation multirate repetitive control for PWM inverters," *IEEE Trans. Ind. Electron.*, vol. 64, no. 9, pp. 7132–7140, Sep. 2017.
[31] Y. Chen, K. Zhou, C. Tang, Y. Shu, and Y. Yang, "Fractional-order multiperiodic odd-harmonic repetitive control of programmable AC power sources," *IEEE Trans. Power Electron.*, vol. 37, no. 7, pp. 7751–7758, Jul. 2022.
[32] C. Tan, Q. Chen, L. Zhang, and K. Zhou, "Frequency-adaptive repetitive control for three-phase four-leg V2G inverters," *IEEE Trans. Transp. Electrific.*, vol. 7, no. 4, pp. 2095–2103, Dec. 2021.
[33] P. Cui, Q. Wang, G. Zhang, and Q. Gao, "Hybrid fractional repetitive control for magnetically suspended rotor systems," *IEEE Trans. Ind. Electron.*, vol. 65, no. 4, pp. 3491–3498, Apr. 2018.
[34] L. Li, L. Xie, W.-Y. Yan, and Y. C. Soh, "Design of low-order linear-phase IIR filters via orthogonal projection," *IEEE Trans. Signal Process.*, vol. 47, no. 2, pp. 448–457, Feb. 1999.
[35] S. Jiang, D. Cao, Y. Li, J. Liu, and F. Z. Peng, "Low THD, fast transient, and cost-effective synchronous-frame repetitive controller for three-phase UPS inverters," *IEEE Trans. Power Electron.*, vol. 27, no. 6, pp. 2994–3005, Jun. 2012.
[36] T. I. Laakso, V. Valimaki, M. Karjalainen, and U. K. Laine, "Splitting the unit delay [FIR/all pass filters design]," *IEEE Signal Process. Mag.*, vol. 13, no. 1, pp. 30–60, Jan. 1996.
[37] J.-P. Thiran, "Recursive digital filters with maximally flat group delay," *IEEE Trans. Circuits Theory*, vol. 18, no. 6, pp. 659–664, Nov. 1971.
[38] S. Chen, Q. Zhao, Y. Ye, and B. Qu, "Using IIR filter in fractional order phase lead compensation PIMR-RC for grid-tied inverters," *IEEE Trans. Ind. Electron.*, vol. 70, no. 9, pp. 9399–9409, Sep. 2023.
[39] Q. Zhao, H. Zhang, Y. Gao, S. Chen, and Y. Wang, "Novel fractional-order repetitive controller based on Thiran IIR filter for grid-connected inverters," *IEEE Access*, vol. 10, pp. 82015–82024, 2022.
[40] J. Ye, L. Liu, J. Xu, and A. Shen, "Frequency adaptive proportional-repetitive control for grid-connected inverters," *IEEE Trans. Ind. Electron.*, vol. 68, no. 9, pp. 7965–7974, Sep. 2021.
[41] M. Zhu, Y. Ye, Y. Xiong, and Q. Zhao, "Parameter robustness improvement for repetitive control in grid-tied inverters using an IIR filter," *IEEE Trans. Power Electron.*, vol. 36, no. 7, pp. 8454–8463, Jul. 2021.
[42] C. D. Olds, *Continued Fractions*. Washington, DC, USA: Math. Assoc. Amer., 1963.
[43] M. Abramowitz and I. A. Stegun, *Handbook of Mathematical Functions*. New York, NY, USA: Dover, 1972.
[44] S. Koshita, M. Abe, and M. Kawamata, "A simple ladder realization of maximally flat allpass fractional delay filters," *IEEE Trans. Circuits Syst. II, Exp. Briefs*, vol. 61, no. 3, pp. 203–207, Mar. 2014.

Pu Liu was born in Baoding, Hebei, China. He received the M.S. degree in computer and electrical engineering from the University of Shanghai for Science and Technology, Shanghai, China, in 2010, and the Ph.D. degree in electrical engineering from Xi'an Jiaotong University, Xi'an, China, in 2016.

From 2016 to 2019, he was a Lecturer with the Xi'an University of Technology, Xi'an, China. Since 2019, he has been with the Zhengzhou University of Light Industry, Zhengzhou, China. His research interests include voltage source converter high voltage

Cong Wang was born in Henan, China. She received the B.S. degree in electrical engineering from Henan University of Engineering, Zhengzhou, China, in 2021. She is currently working toward the M.S. degree in electrical engineering with the Zhengzhou University of Light Industry, Zhengzhou, China.

Her research interests include renewable energy systems and grid-connected inverters.

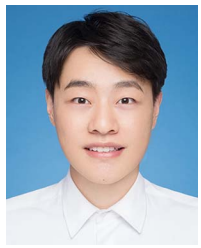

Yingwei Zhang was born in Handan, Hebei, China. He received the B.S. degree in electrical engineering in 2020 from the University of Shanghai for Science and Technology, Shanghai, China, where he is currently working toward the M.S. degree in electrical engineering.

His current research interests include power converters for renewable energy applications and control of power electronics.

Yan Liang was born in Yangquan, Shanxi, China. She received the M.S. degree in computer and electrical engineering from the University of Shanghai for Science and Technology, Shanghai, China, in 2009.

She was with XJ Group Corporation, Xuchang, China. She is currently a Research Fellow with Zhengzhou University of Light Industry, Zhengzhou, China. Her research interests include wireless power transfer and renewable energy integration.

Yibo Cui was born in Henan, China. He received the B.S. degree in electrical engineering in 2021 from Zhengzhou University of Light Industry, Zhengzhou, China, where he is currently working toward the M.S. degree in electrical engineering.

His research interests include renewable energy systems and sensorless control for ac motors.

Jie Fang received the B.S. degree in electrical engineering and the M.S. degree in electrician theory and new technology from Zhengzhou University, Zhengzhou, China, in 2002 and 2007, respectively, and the Ph.D. degree in control engineering from the Nanjing University of Aeronautics and Astronautics, Nanjing, China, in 2012.

She is currently a Professor with the School of Electrical and Information Engineering, Zhengzhou University of Light Industry, Zhengzhou, China. Her research interests include nonlinear control theory and applications and complex network control.